Title

Water Adsorption on Mica Surfaces with Hydrophilicity Tuned by Counterion Types (Na, K, and Cs) and Structural Fluorination

Journal

The Journal of Physical Chemistry C, 126(38)

ISSN

1932-7447

Authors

Koishi, Ayumi

Lee, Sang Soo

Fenter, Paul

et al.

Publication Date

2022-09-29

DOI

10.1021/acs.jpcc.2c04751

Water Adsorption on Mica Surfaces with Hydrophilicity Tuned by Counterion Type (Na, K, Cs) and Structural Fluorination

Ayumi Koishi,[1,*,#] Sang Soo Lee,[2,*] Paul Fenter,[2] Alejandro Fernandez-Martinez,[3] Ian C. Bourg[1,4]

[1]Department of Civil and Environmental Engineering, Princeton University, Princeton, New Jersey 08544, United States

[2]Chemical Sciences and Engineering Division, Argonne National Laboratory, 9700 South Cass Avenue, Lemont, Illinois 60439, United States

[3]Université Grenoble Alpes, Université Savoie Mont Blanc, CNRS, IRD, IFSTTAR, ISTerre, 38000 Grenoble, France

[4]High Meadows Environmental Institute, Princeton University, Princeton, New Jersey 08544, United States

KEYWORDS. Adsorption, water, thin film, mica, hydrophilicity.

ABSTRACT: The stability of adsorbed water films on mineral surfaces has far-reaching implications in the Earth, environmental, and materials sciences. Here, we use the basal plane of phlogopite mica, an atomically smooth surface of a natural mineral, to investigate water film structure and stability as a function of two features that modulate surface hydrophilicity: the type of adsorbed counterion (Na, K, Cs) and the substitution of structural OH groups by F atoms. We use molecular dynamics (MD) simulations combined with in situ high-resolution X-ray reflectivity to examine surface hydration over a range of water loadings, from the adsorption of isolated water molecules to the formation of clusters and films. We identify four regimes characterized by distinct adsorption energetics and different sensitivities to cation type and mineral fluorination: from 0 to ½ monolayer film thickness, the hydration of adsorbed ions; from ½ to 1 monolayer, the hydration of uncharged regions of the siloxane surface; from 1 to 1½ monolayer, the attachment of isolated water molecules on the surface of the first monolayer; and for > 1½ monolayer, the formation of an incipient electrical double layer at the mineral-water interface.

INTRODUCTION

How does the stability of thin liquid water films adsorbed at mineral-air interfaces depend on the atomic-level structure of the underlying solid? This question has important implications in the Earth sciences, for example in soil hydrology [1–4], aerosol chemistry [5–8], and the storage of CO_2 and hazardous wastes in geologic formations [9–11]. It also impacts the development of technologies such as electrowetting devices [12] and fouling-resistant membranes [13]. Closely related questions regarding the stability of thin water films confined between solid surfaces recur in a variety of systems, for example in intracellular environments [14,15], colloidal suspensions [16–18], biological channels [19], and geologic media [20,21].

The question posed above persists, despite more than a half-century of studies [22–25], mainly because of significant experimental challenges. In particular, whereas recent advances in synchrotron-based X-ray reflectivity (XRR), atomic force microscopy (AFM), and other techniques now enable direct observations of the atomic-scale structure of the hydration layers at the mineral–*bulk* liquid water interfaces [26–29], equivalent characterization of water in thin adsorbed films remains arduous, notably because of the difficulty of precisely controlling film thickness in the presence of adventitious carbon [30–32], formation of reactive radicals [33–35], or capillary interactions [36–38]. Consequently, knowledge of the nanoscale properties of water in thin adsorbed films remains comparatively limited. The *experimental* database consists largely of bulk measurements of thermodynamic properties as a function of film thickness, notably based on adsorption isotherms and calorimetry measurements [39–44]. These are supplemented by a small but rapidly-growing number of atomic-level observations achieved using X-ray photoelectron spectroscopy (XPS) [45,46], infrared spectroscopy [6,8,10,39], sum frequency generation spectroscopy [22,47,48], and frequency-modulation AFM [49].

Because of the experimental challenges outlined above, existing studies of adsorbed water films on mineral surfaces have relied extensively on *computational* techniques including density functional theory (DFT) and molecular dynamics (MD) simulations [11,23,58–60,50–57]. A subset of these studies reported characterizations of both nanoscale structure and adsorption energetics (e.g., free energy and/or enthalpy of water adsorption) as required to fundamentally elucidate the hydrophilicity of the mineral surfaces [23,50–57,60]. It must be noted, however, that this reliance on MD simulations presents risks, as the inter-atomic interaction potential models used in these simulations have only been sparsely tested for systems that contain a thin water film adsorbed on a mineral surface.

A second reason for the persistence of the question posed above is the relatively limited number of detailed comparisons of water adsorption on different mineral surfaces. While many studies have examined water films on a single surface, including notably on muscovite mica [23,49,61] and metal or metal oxides [45,62–65], few have systematically compared water films on a series of surfaces with controlled differences in composition. To the best of our knowledge, only four studies, all relying primarily on MD simulations, have compared the stability of adsorbed

water films on different mineral surfaces (i.e., Wang et al. [54]; Rotenberg et al. [50]; Phan et al. [59]; Fernandez-Martinez et al. [55]). These studies examined atomistic-level structure and energetics in water films with thickness up to ~3 nm on the surfaces of brucite, gibbsite, hydrotalcite, muscovite, talc, fluorotalc, pyrophyllite, quartz, and imogolite.

A key result of previous studies, and particularly of the four MD simulation studies noted above, is that the first (and in some cases the second) water monolayers adsorbed on mineral surfaces are highly distinct from bulk liquid water both structurally and energetically. The properties of water in these monolayers are strongly impacted by (i) the density and orientation of surface OH groups, (ii) the density of mineral surface charge, and (iii) the type of adsorbed counterions, i.e., by features that determine the polarity of the mineral surface. These features influence the stability of adsorbed water films through changes in the overall hydrophilicity of the mineral surface by moderating the competition between adhesion (favorable water-surface interactions) and cohesion (favorable water-water interactions) in the water films on the mineral surfaces [50]. These observations of a highly distinct structure and energetics of the first two water layers adsorbed on mineral surfaces are reminiscent of the distinction between the Stern and diffuse layers in classical models of adsorption and charge screening at mineral-water interfaces, where the Stern layer is generally associated with the first two water monolayers in which ions adsorb as inner- and outer-sphere surface complexes, suggesting parallels between water adsorption at mineral-air interfaces in unsaturated systems (the focus of the present study) and the broader topic of ion adsorption at mineral-water interfaces.

Here, we build upon previous MD simulation studies of adsorbed water films on mineral surfaces by carrying out a comparative study of film structure and energetics on various surfaces. Our methodology diverges from those used in previous MD simulation studies in several ways. First, we complement our simulations with XRR measurements that provide information at length scales that are directly comparable to simulations at high water coverages in an effort to establish the accuracy of our simulation predictions. Second, we carry out additional characterization of the thermodynamics of water adsorption, notably by calculating both the enthalpy and free energy of adsorption, comparing several methods of calculation of the free energy of adsorption, and comparing our results with experimental water adsorption isotherms. Third, rather than contrasting water adsorption on very different minerals, as in Wang et al. [54] and Phan et al. [59], we compare water adsorption on several variants of a same mineral, as in Rotenberg et al. [50] and Fernandez-Martinez et al. [55]. Specifically, we examine water films on six types of phlogopite mica where mineral surface hydrophilicity is modulated by varying the identity of adsorbed counterions (Na, K, or Cs) and of structural OH or F groups in the mineral framework. We focus particularly on the links between structure and energetics during the uptake of the first two adsorbed water monolayers.

MATERIALS AND METHODS

Mineral Structure. Phlogopite, $KMg_3(Si_3Al)O_{10}(F,OH)_2$, is the Mg end-member of trioctahedral mica (biotite). This mineral has a 2:1 phyllosilicate structure consisting of a sheet of MgO_6 octahedra sandwiched between two sheets of SiO_4 tetrahedra (Fig. 1a) with all three octahedral sites occupied by Mg (trioctahedral). In comparison, the more extensively examined muscovite mica has Al in two-thirds of the octahedral sites (dioctahedral). In the ideal structure, ¼ of the Si atoms in the tetrahedral sheets are substituted by Al, resulting in a net negative charge within the layer that is compensated by interlayer K^+ ions.

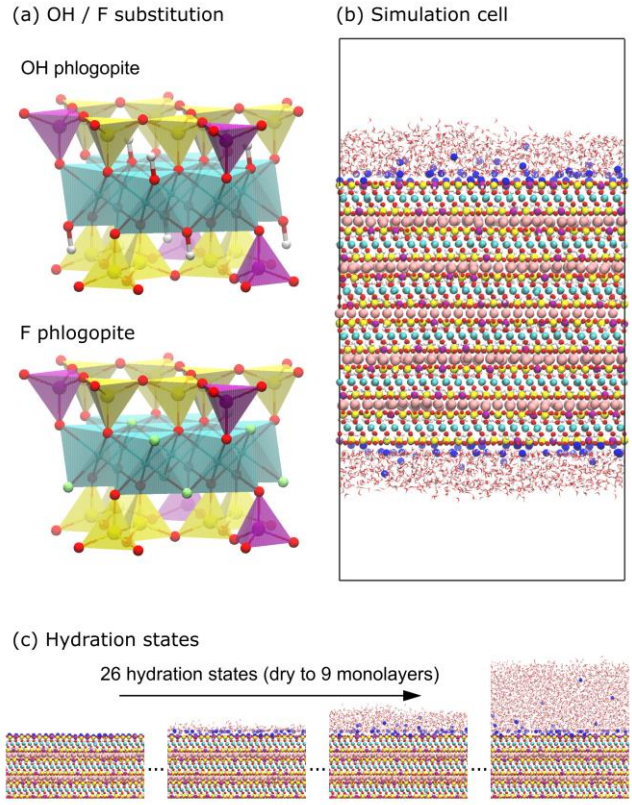

Figure 1. (a) Structure models of phlogopite without and with fluorine substitution (yellow, purple, and cyan polyhedra: SiO_4, AlO_4, and MgO_6; red, white, and light green spheres: O, H, and F atoms). (b) Simulation snapshot showing adsorbed water films (red and white sticks) with a thickness of three water monolayers (3 ML) on the basal surfaces of a 6-nm-thick slab of Na-bearing OH phlogopite (pink and dark blue spheres: charge-balancing K ions in the interlayers and Na ions on the external basal surfaces, respectively). (c) Snapshots of the simulation of Na-bearing OH phlogopite at various hydration states. Phlogopite-water interaction was studied over a total of 26 hydration states from dry to 9 ML.

The phyllosilicate basal surface examined here is common to the micas and clay minerals and has been extensively examined as a reference surface in the Earth and interfacial sciences [27,66–71]. It exposes an atomically smooth plane of siloxane O atoms formed by the bases of corner-sharing SiO_4 tetrahedra. A notable feature of this surface is the existence of distorted hexagonal (more precisely, ditrigonal) cavities formed by rings of six surface O atoms. On phlogopite mica, these cavities are more closely hexagonal (i.e., less distorted) than on muscovite [72,73], with potential subtle impacts on the adsorption of exchangeable cations as inner-sphere surface complexes above these cavities. A second notable feature of phlogopite (and other micas) is that the random distribution of isomorphic substitutions of Si by Al near the mineral surface causes a non-uniform surface charge distribution: half of the surface O atoms carry more negative charge due to nearby isomorphic substitutions, and surface

hexagonal cavities are bordered by either 0, 1, 2, or 3 isomorphic substitutions.

Here, we examine the sensitivity of adsorbed water on phlogopite mica to two features that influence the hydrophilicity of the siloxane surface. The first is the identity of the exchangeable cations that balance the mica surface charge. More specifically, we examine the influence of three different alkali metals (Na, K, Cs) with increasing radius and decreasing hydration energy. The second is the presence of substitutions of OH by F within the mica structure, directly below the hexagonal cavities of the basal surface. This substitution is common in phyllosilicates [74,75] and is known to modulate wetting properties [50,76,77], mineral stability [74,78,79], and electrical conductivity [80]. The present study considers the two end members: fully hydroxylated or fully fluorinated phlogopite, referred to hereafter as OH or F phlogopite, respectively (Fig. 1a).

Molecular Dynamics Simulations. Simulated systems consisted of a 60 Å-thick phlogopite slab without or with fluorine substitution—$KMg_3(AlSi_3O_{10})(OH)_2$ and $KMg_3(AlSi_3O_{10})F_2$, respectively—in a 63.84 × 55.26 × 120 to 160 $Å^3$ simulation cell with periodic boundary conditions. Both mica basal surfaces were coated with an adsorbed water film with a thickness of 0 to 9 monolayers (ML) (Fig. 1b and 1c). One monolayer is defined as 5.25 water molecules per unit cell surface area (48.997 $Å^2$) based on the bulk water density. The simulation cell size in the *z* direction was selected such that the two water films did not interact with each other. Isomorphic substitutions of Si by Al were randomly distributed within each tetrahedral layer while avoiding neighboring substitutions. This generated on average 8.3, 39.9, 45.3, and 6.5% of cavities bordered by 0, 1, 2, or 3 isomorphic substitutions, respectively, and this same structure was used for the entire work. For both OH and F phlogopite, three systems were simulated with K, Na, and Cs counterions compensating the surface charge of the mineral (i.e., one cation per unit cell surface area), yielding a total of 6 systems. Each system was studied for a total of 26 hydration states generated as follows with a fixed number of counterions as required for charge balance. First, each system was equilibrated at hydration states of 3, 6, and 9 ML for 1.5 ns in the *NVT* ensemble (including 250 ps of annealing at 343 K to facilitate the establishment of a well-equilibrated counterion distribution), followed by a short (50 ps) structure relaxation (*x*-*y* directions) in the *NPT* ensemble and finally by 0.5 ns of equilibration in the *NVT* ensemble. Then, hydration states below 3 ML were generated by removing randomly selected water molecules from the 3 ML system, with each water removal being followed by 0.5 ns of equilibration and 0.5 ns of simulation before the next water removal step. Finally, each state was simulated for an additional 2.5 ns in the *NVT* ensemble for data production. All simulations were carried out at 298 K using a Nose-Hoover thermostat. Equations of motion were solved using the Verlet algorithm with a 1 fs time step for all atoms except for a single plane of interlayer K ions at the mid-plane of the phlogopite slab that was kept immobile and water molecules kept rigid using the SHAKE algorithm [81]. For calculations of water chemical potential and relative humidity (refer to following paragraphs), a selected set of states was simulated for 40 ns.

Interatomic interactions were modeled using the SPC model for water molecules [82], the CLAYFF model for phlogopite [83], and the Dang model for alkali metal ions [84]. As the CLAYFF model does not include parameters for fluorine in phyllosilicate minerals, we modeled structural F atoms using a strategy by Marry, Rotenberg, and coworkers [50,85] whereby a charge equal to that of the OH group (-0.525 eV) is assigned to F with Lennard-Jones parameters of the fluoride ion [86]. Although the SPC/E water model has been more extensively validated in conjunction with the CLAYFF model in studies of phyllosilicate minerals [28,85,87,88], the SPC model was used here both because it was initially used in the development of the CLAYFF model and because it predicts a more accurate vapor pressure at 298 K [89,90], which enabled a more precise determination of the relationship between relative humidity and water film thickness. Interatomic interactions were resolved in real space up to 12 Å. Long-range Coulomb interactions beyond 12 Å were resolved in reciprocal space using the particle-particle/particle-mesh (PPPM) technique with an accuracy of 99.99%. Simulations were carried out on the Cori supercomputer at the National Energy Research Scientific Computing Center (NERSC) using the code LAMMPS [91].

Two energetic properties were computed for each hydration state: the differential enthalpy $\Delta H_{ads}(N)$ and free energy $\Delta G_{ads}(N)$ associated with the adsorption of a single water molecule to a surface at a given hydration state *N*. The adsorption enthalpy was determined from the potential energy of the system under the assumption that internal energy *U* is mostly due to intermolecular potential energies and that the $P\Delta V$ term is negligibly small at near-ambient pressures [54], such that $\Delta H_{ads}(N) \approx dE_{pot}/dN$ at any water content *N*, where E_{pot} is the total potential energy due to intermolecular interactions predicted by our simulations. Reported ΔH_{ads} values were calculated from the slopes obtained by linear regression using the nearest three potential energy data points. For ΔG_{ads}, reported values were calculated based on observations of water evaporation during 40 ns simulations carried out at selected film thicknesses. More precisely, adsorption free energy was calculated as $\Delta G_{ads}(N) \approx \Delta F_{ads}(N) = RT\ln(\rho_{void}/\rho_0)$, where *R* is the ideal gas constant, *T* is the temperature in K, and ρ_{void} and ρ_0 are average water densities in the vapor phase (i.e., in the void region) and in bulk liquid water. The small difference between Gibbs (*G*) and Helmholtz (*F*) free energies is negligible at near-ambient pressure. The differential adsorption free energy $\Delta G_{ads}(N)$ was used to determine the relative humidity of each simulated system using the relation $RH(N) = \exp[(\Delta G_{ads}(N) - \Delta G_0)/RT]$, where ΔG_0 is the free energy of condensation of water obtained by simulating a system containing a slab of bulk-liquid-like water (with 1800 water molecules) in contact with water vapor for 120 ns in a 30 × 30 × 90 $Å^3$ periodic simulation cell (ΔH_{ads} for bulk liquid water is also obtained from this separate simulation). At low surface coverages, the number of evaporation events observed during 40 ns of simulation was too low to precisely determine ρ_{void}. To circumvent this challenge and to cross-validate our calculations, hybrid Grand Canonical Monte Carlo and MD (GCMC+MD) simulations were conducted at 2 and 5% RH to determine the equilibrium surface water coverage at a fixed water chemical potential (refer to Supporting Information).

Finally, we performed a bond valence (BV) analysis [92] of ion coordination as a function of film thickness. The BV approach, initially developed for studies of crystal structures, defines a semi-empirical bond valence associated with all pair-wise coordination interactions based on the empirical function $s_{ij}(r) = \exp((r_0-r_{ij})/B)$, where r_{ij} is the distance between a pair of atoms *i* and *j* and r_0 and *B* are empirical parameters, specific to a given pair, obtained by fitting to a large number of mineral structures [93]. Specifically, we followed the approach of Bickmore et al. [94],

whereby the bond valence s_{ij} associated with the average coordination of atoms of type i by all atoms of type j is evaluated from the corresponding radial distribution function $g_{ij}(r)$:

$$s_{ij} = \int_0^{r_1} g_{ij}(r) s_{ij}(r) \rho_j 4\pi r^2 \mathrm{d}r$$

where r_{min} is the first minimum of $g_{ij}(r)$ and ρ_j is the number density of atom j in the simulation cell. We used B = 0.37 and r_0 values by Bickmore et al. [94] for H-O pairs and by Brown and Altermatt [93] for all other cation-anion pairs.

X-ray Reflectivity Experiments. In order to validate our choice of interaction parameters for structural F atoms in the simulation, X-ray reflectivity (XRR) measurements were conducted at the 33-ID-D beamline at the Advanced Photon Source (Argonne National Laboratory, USA). A synthetic F phlogopite crystal ($KMg_3(AlSi_3)O_{10}F_2$; H.C. Materials corporation, IL, USA) was cleaved using tape in ultrapure water to minimize the splitting force. The freshly cleaved crystal was then mounted in an X-ray thin-film cell where aqueous solutions (9 mM MCl, with M = Na, K, or Cs) were injected and allowed to react for at least 30 min. The excess solution was drained, and a several-micrometers-thick solution film was maintained on top of the sample. The sample cell was mounted in a Newport 6-circle diffractometer for X-ray experiments. A monochromatic X-ray beam (at 14.0 keV) reflected from the sample surface was collected using a Pilatus 100K area detector as a function of momentum transfer q, defined as $q = 4\pi \sin(2\theta/2)/\lambda$, where 2θ is the angle between the incident and reflected X-ray beams and λ is the wavelength of the X-rays (0.886 Å).

The experimental and data analysis methodologies have been described in previous studies [28,95]. Briefly, XRR data were analyzed using a structural model consisting of the phlogopite mica structure with the top three 2:1 layers (~30 Å in depth) allowed to relax vertically, the interfacial solution profile, and bulk water. The bulk mica structure was obtained from the single-crystal X-ray diffraction analysis of the F phlogopite (data obtained at Diamond I19). A mica model with structural relaxation allowed in the top four 2:1 layers was also tested but showed no substantial improvement in the quality of fit based on the χ^2 criterion defined in the next paragraph. In addition, the vertical relaxation remains small and mostly limited to the topmost 2:1 layer (Fig. S2) as expected from the less distorted hexagonal cavities in phlogopite mica (trioctahedral) as compared to muscovite mica (dioctahedral) [28,72,73,96]. The initial interfacial solution structure was derived from the MD simulation for each system at the highest water loading (i.e., 9 ML). A parameter Δz_{MD} (Table S1) was used to express the vertical displacement of the MD-derived profile from the average position of the surface oxygen atoms from which the height z is defined. This interfacial solution structure was further optimized by including multiple Gaussian peaks with varying occupancy factors (either positive or negative), heights, and rms widths (≥0.2 Å, where the minimum was set to prevent convergence to unreasonably small values) as a simplistic approach where the summation of the peaks provides the difference in total electron density between the MD-derived profile and best-fit model. The derived differential electron-density profile expressed the electron density that was under- or over-estimated by the simulations. The statistical uncertainty of the differential profile was calculated using error propagation (see Supporting Information for details). The resulting profiles were statistically well constrained (i.e., within the level of the 2-σ uncertainty that was mostly smaller than ~20% of the solution density; Fig. S3) even when some parameters of the Gaussian peaks were determined with strong negative covariance (i.e., >99%). The individual profiles are reported as a separate supporting document. The bulk water structure was expressed using an error function.

Model parameters were optimized using least-squares fitting. The best-fit model was selected based on the smallest χ^2 (= $\Sigma_k[(I_k - I_{calc,k})/\sigma_k]^2/(N-N_p)$, where I_k and $I_{calc,k}$ are the measured and calculated intensities, respectively, σ_k is the measured uncertainty of the k^{th} data point, and N and N_p are the numbers of data points and parameters used in the model-fit, respectively). The R-factor (= $\Sigma_k(|I_k - I_{calc,k}|/I_k)/N$) of the best-fit was also reported for comparison.

RESULTS AND DISCUSSION

Water Density Profiles. Figure 2 presents MD simulation predictions of the density profiles of water O atoms as a function of distance from the surface of OH or F phlogopite with Na, K, or Cs exchangeable cations (hereafter referred to as M-OH/F phlogopite, where M = Na, K, or Cs). Predicted density profiles at the highest water coverage (9 ML) are broadly consistent with previous observations of water in contact with OH muscovite mica [28,54,97–99]. Water density peaks corresponding to the first, second, third, and fourth water monolayers are located at z = 2.66 ± 0.04, 6.17 ± 0.35, 9.13 ± 0.05, and 11.81 ± 0.03 Å relative to the plane of surface O atoms (95% confidence intervals calculated across all systems at 9 ML water coverage). The extent (12 Å) and periodicity (3 Å) of the water density layering are also consistent with previous studies [98,100,101]. Water density in the first monolayer is subdivided into three features—a peak or shoulder at z = 1.74 ± 0.05 (denoted 1a in Fig. 2), a main peak at z = 2.66 ± 0.04 (1b), and a peak or shoulder at z = 3.78 ± 0.24 Å (1c)—that reflect first-layer water molecules that donate either two, one, or zero hydrogen bonds to surface O atoms, respectively [28,102]. Water density in the second monolayer shows evidence of subdivision into two features, most obviously in the Na- and K-OH phlogopite systems, where water molecules have preferred locations at z = 5.2 ± 0.17 and 6.29 ± 0.22 Å (Figs. 2a and 2b), perhaps reflecting the fact that only half of the surface hexagonal cavities carry an adsorbed counterion. In the Cs-OH and Cs-F systems, the first subcomponent appears to be connected more to the third feature in the first monolayer rather than to the second subcomponent in the second monolayer. Subdivision is least obvious for Na- and K-F phlogopite systems.

Comparison of the different simulated systems at the highest water coverage reveals that structural OH/F and adsorbed cation significantly impact water density distribution in the first two monolayers. In particular, the main density peak at 2.7 Å (1b) is strongly attenuated in the presence of either structural F or with the larger counterions (Figs. 2 and S4), while the shoulder at 1.7 Å (1a) becomes enhanced and the shoulder or peak at ~3.8 Å (1c) becomes enhanced and shifted to higher z coordinates under these conditions. This sensitivity of water density layering to surface structure is observed only for the two water layers closest to the mineral surface, in agreement with studies indicating that the impacts of solutes or surfaces on water coordination and reorientational dynamics are generally discernible over distances of no more than two water layers [101,103,104]. Our results imply that the Stern layer is not simply a passive locus of ion adsorption; instead, the structure of water in this layer is significantly impacted by the identity of the adsorbed cation.

We note, in passing, that the peak or shoulder at 1.7 Å (1a), which corresponds to water molecules located above the hexagonal cavities of the siloxane surface and donating hydrogen bonds to two surface O atoms, is a sensitive indicator of the presence and orientation of structural OH groups within the cavities. Based on Fig. 2 and our previous results for muscovite mica [28], the intensity of this peak progressively increases from OH phlogopite (where structural OH groups are oriented nearly normal to the surface) to OH muscovite (where structural OH groups are oriented at a ~30° angle to the surface) to F phlogopite (where structural OH groups are absent), i.e., it varies inversely with the magnitude of the dipole moment of the OH groups in the direction normal to the surface (z). Dipole-dipole repulsive interaction likely frustrates the adsorption of these particular water molecules donating two hydrogen bonds in presence of the structural OH groups.

Results at lower hydration levels in Fig. 2 reveal that the growth of the adsorbed water film proceeds initially through the adsorption of water molecules that donate either one or two hydrogen bonds to surface O atoms (peak 1b and shoulder 1a at 0.1 and 0.3 ML in Fig. 2). The growth of the main density peak is initially more rapid in the case of larger and less strongly hydrated counterions (Cs > K > Na at 0.3 ML), particularly in the OH phlogopite system. As hydration increases from 0.3 to 1 ML, additional first-layer water molecules are predominantly added to peak 1b on Na-phlogopite, whereas they are more significantly added to peak 1c on K- or Cs-phlogopite. Because of this difference, the order of first peak heights undergoes a reversal (to Na > K > Cs) as hydration increases from 0.3 to 1 ML. Beyond the first water monolayer, adsorption of additional water monolayers proceeds in a layer-by-layer manner with the adsorption of each additional layer having little or no influence on the structure of previously adsorbed water layers. The only significant exception is the adsorption of the second water layer, which causes a minor redistribution of first-layer water from peak 1b to shoulder 1a.

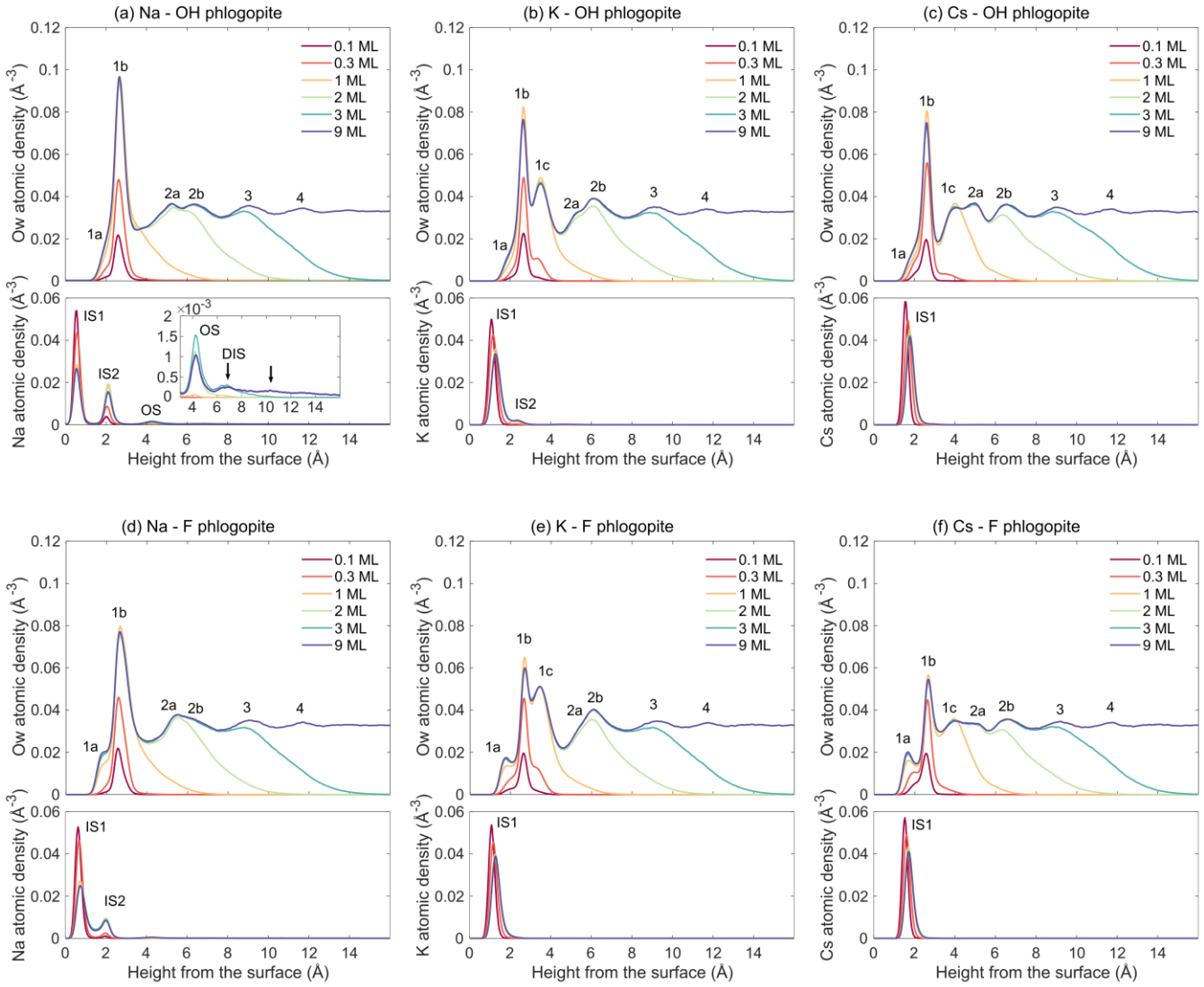

Figure 2. Water O atom and counterion (Na, K, or Cs) density profiles as a function of distance from the mica surface (more precisely, as a function of distance from the average z coordinate of siloxane surface O atoms) for selected surface water coverages from 0.1 to 9 monolayers

(ML). Numbers indicate the different density peaks or shoulders in the first, second, third, and fourth water layers and the different species of adsorbed ions (see text).

Counterion Density Profiles. In addition to the water O atomic density profiles, Figure 2 also presents the density profiles of Na, K, and Cs counterions on OH and F phlogopite. In agreement with previous studies of muscovite mica, our results indicate that exchangeable cations adsorb predominantly as two distinct types of inner-sphere (IS) surface complexes [28,105]. The first density peak (IS1), located at z = 0.54 to 0.75 Å for Na, 1.27 to 1.29 Å for K, and 1.74 to 1.80 Å for Cs at 9 ML water coverage on OH and F phlogopite, corresponds to cations located above hexagonal cavities of the siloxane surface. The second peak (IS2), at z = 2.03 to 2.10 Å for Na, 2.35 to 2.37 Å for K, and absent for Cs, corresponds to cations located above 'triads' of surface O atoms that coordinate an isomorphic substitution. In addition to these inner-sphere surface complexes, the results presented in Fig. 2 demonstrate the existence of a small population of outer-sphere (OS) surface complexes, visible notably in the Na density peak at z = 4.26 to 4.29 Å, and a faint diffuse ion swarm (DIS), i.e., non-zero counterion density beyond the second water layer (Fig. 2a inset, also discernible in the fourth panel in Fig. 1c) in agreement with classical theories of ion adsorption at charged interfaces [106,107] and with previous observations for a variety of surfaces [28,108,109].

Comparison of the cation density profiles at the highest water coverage indicates that the IS1 complex is the predominant species for all cations. The relative importance of the IS2 complex increases in the order Cs < K < Na and F < OH. The dependence on cation size is consistent with that observed for muscovite mica, where large ions (K, Rb, Cs) predominantly form IS1 species whereas small ions (Li, Na) prefer IS2 and the z-coordinates of the IS species increase with the ionic radius [28,105]. The main difference relative to previous observations for muscovite is the generally greater importance of IS1 for phlogopite, i.e., cations are more predominantly adsorbed within the hexagonal cavities of the siloxane surface. This difference may be related to the larger effective radius of these cavities on phlogopite (where the cavities are more hexagonal) than on muscovite (where they adopt a distinctly ditrigonal shape) [72,73]. In the case of F phlogopite, the absence of structural OH groups can further facilitate cation adsorption in the cavity sites by reducing steric (and presumably electrostatic as discussed above) hindrance between the hydrogen and the adsorbed cation. This is particularly clear for Na ions on F phlogopite, for which the presence of the OS species is negligible compared to those on OH phlogopite (Fig. S4b). Similarly, K ions on F phlogopite form no IS2 species, unlike those on OH phlogopite.

Finally, Figure 2 reveals the evolution of counterion density profiles as a function of water film thickness, which, to the best of our knowledge, has rarely been reported in the literature [56]. In the K and Cs systems, water film thickness has little impact on adsorbed cation speciation (which is consistently dominated by the IS1 species), but the IS1 density peak becomes broader and shifts away from the surface (by 0.22 ± 0.03 Å) with increasing film thickness. In contrast, on Na-exchanged phlogopite, the location of the cation density peaks varies minimally with water film thickness, but the speciation shows a significant shift from IS1 towards IS2 and OS species with increasing film thickness. While the peak shift observed for the K system is in qualitative agreement with Adapa et al. [56], their predictions for the Na ion densities indicate significant peak shift and do not exhibit different surface species.

Comparison Between MD and XRR Results. The validity of the interfacial solution structures obtained by MD simulations was tested by comparing experimental XRR data with the patterns calculated from the MD-derived profiles (Fig. 3). The calculation was conducted for the Na, K, and Cs systems determined using the highest water loading (9 ML). The experimental data were collected with F phlogopite (001) in 9 mM alkali metal chloride solutions.

The comparison between the measured and calculated XRR data shows generally good agreement, indicating that the MD-derived profiles well represent the overall solution structure in the experimental systems, including the location of adsorbed cations and primary hydration layers. This validates the overall accuracy of the force-field parameters used for the F atoms in the simulation. However, statistically significant deviations are observed around the q values where the reflectivities are the lowest, i.e., where the data are most sensitive to small differences in interfacial structure (Fig. 3). These differences imply that the predicted interfacial structure is less accurate in fine details. For the Na-F phlogopite system, the direct MD–XRR comparison yields a moderate agreement (χ^2 = 27.6 and R-factor = 16%) where the largest discrepancy was observed for data in q = 4.5–4.9 Å^{-1} (Fig. 3a). The optimization of the structure by considering under- or over-estimated electron densities in the interfacial solution structure improved the agreement (χ^2 = 5.7 and R-factor = 8%) and shows that the difference is mostly due to the underestimation of the degree of ordering of the interfacial hydration layers (Fig. 3d). For example, the electron density of the adsorbed water layers at ~1.4, 2.6, and ~4.9 Å is less pronounced in the MD-derived profile. A similar tendency is observed for the K-F phlogopite system. The agreement between MD and XRR is significantly improved (i.e., χ^2 from 27.8 to 7.3 and R-factor from 15% to 9%) by incorporating additional electron density at ~2.7 and 5.0 Å. At the same time, the MD simulation slightly overestimates the electron density at ~3.5 Å and between 5.5 and 10 Å (Fig. 3e). For the Cs-F phlogopite system, the difference is largely due to the hydration layers at ~1 and 5 Å, consideration of which significantly improves the agreement (i.e., χ^2 from 23.8 to 6.1 and R-factor from 13% to 8%.) This analysis also shows additional electron density at ~2.4 Å, which matches the adsorption height of Cs. Based on the difference in the integrated electron density, we estimate that the coverage of Cs was somewhat higher (by ~17%) than the value (= 1) assumed in the simulation.

While the direct comparison between MD simulations and XRR data validates the general agreement of the interfacial structures determined by the simulations and the experiments, the apparent discrepancies highlight the need for understanding structural differences on finer scales. For all systems, the simulations underestimate the degree and vertical extension of the interfacial ordering of the hydration layers. In particular, distinct electron-density layers are observed at ~5 Å from the mica surface in the optimized structure for all three systems. This underestimated water structure may be related to the difference in ion concentration between the simulation and experiment. For example, the experimental solution contains hydronium, which can compete against the alkali metals for adsorption sites on the mica surface. This effect is likely most significant for Na^+, which is reported to adsorb least strongly to the mica surface among the studied cations [28,110]. This competition effect appears

to be less significant for less strongly hydrated cations and mostly negligible for Cs adsorption on the mica surface. The observed structural difference may also be related to the difference in the magnitude and distribution of the negative charge at the mica surface. For example, the comparison for the Cs system indicates that the coverage of Cs may be underestimated, implying that the surface charge of the mica could be higher for the experiment. This inferred difference in surface charge can stem from the simplistic parameterization assigned to the F atoms in the simulation or from a difference in the isomorphic substitutions between the simulated structure and the sample and may explain the observed fine differences in hydration structure and adsorbed cation speciation.

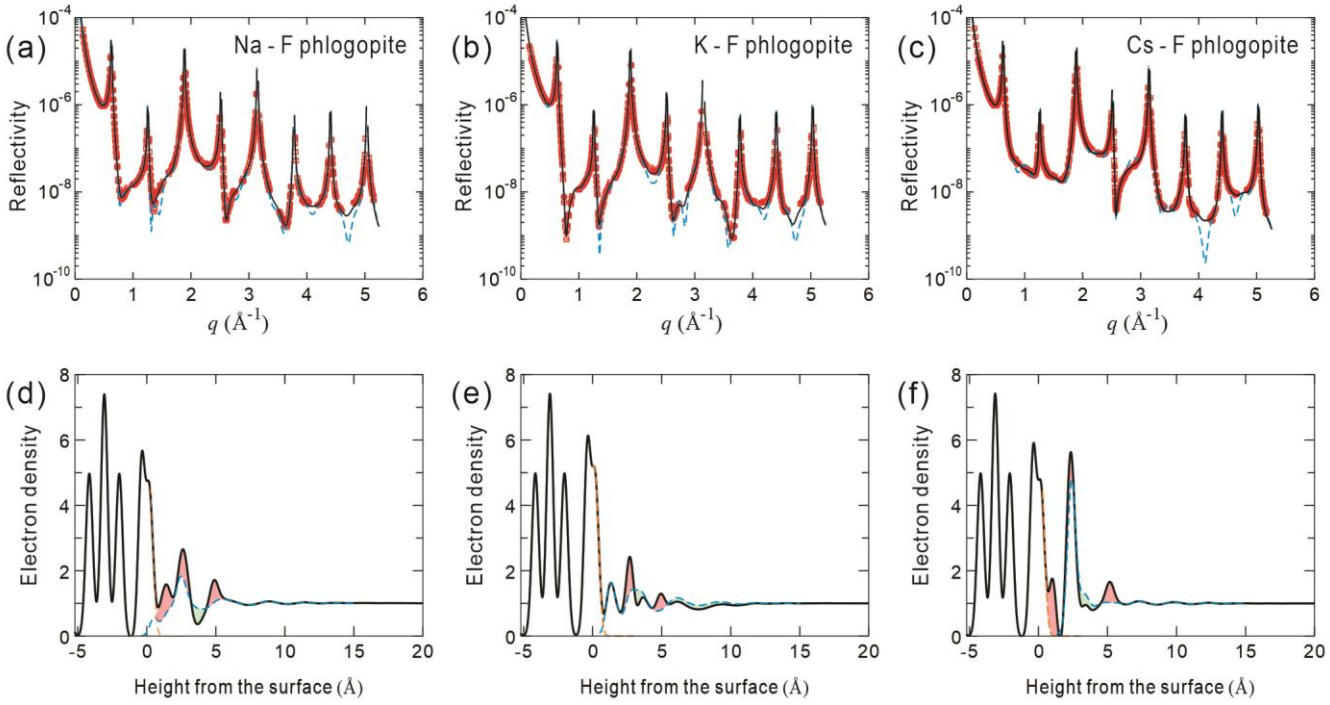

Figure 3. (a–c) In-situ XRR data at the F-phlogopite (001)–9 mM alkali metal chloride solution interfaces. Reflectivity data are shown in red, calculated intensities using MD-derived solution profiles as dashed blue lines, and the best-fit models of the corresponding XRR data as solid black lines. Each analysis includes duplicate datasets (plotted together) measured on different spots on the same crystal surface. (d–f) Comparison of electron density profiles derived from MD simulations (dashed blue lines) and from the best-fit models of the XRR data (solid black lines). Electron density differences between these two profiles are highlighted as shaded pink or green areas to indicate where the best-fit model has a higher or lower electron density than the MD-derived profile, respectively. The electron-density profile of the top oxygen plane of the mica is shown as a dashed orange line. The electron density is normalized to that of bulk water so that the density of water is equal to 1.

Energetics of Water Adsorption. Figure 4 shows the computed change in the differential enthalpy (ΔH_{ads}), free energy (ΔG_{ads}), and entropy ($-T\Delta S_{ads}$, calculated as the difference between ΔG_{ads} and ΔH_{ads}) of adsorption associated with the addition of a single water molecule on Na-, K-, and Cs-bearing OH and F phlogopite covered with n monolayers of water ($0 < n < 3$). For comparison, the average potential energy associated with individual water-water hydrogen bonds in bulk liquid water is about -20 kJ mol^{-1} [111]. The results on ΔG_{ads} vs film thickness presented in Figs. 4a,b are also expressed in Fig. 4c as a relationship between film thickness and relative humidity. Shaded areas in Figs. 4a and 4c indicate experimental values reported for K-muscovite mica [39,41].

As a general trend for all six surfaces, ΔH_{ads} values associated with the addition of a single water molecule on the phlogopite surface are most negative in the dry state and rapidly approach the value for bulk liquid water (horizontal dashed line at -41.0 kJ mol^{-1}, obtained in a separate simulation as described in Materials and Methods) with increasing film thickness. Predictions of ΔH_{ads} vs. film thickness reveal the existence of four distinct hydration regimes. In the first regime, from 0 to ½ ML water coverage, water uptake from pure bulk liquid water is highly exothermic (by -10 to -40 kJ mol^{-1}). This exothermic nature is sensitive to cation type and increases in the order of Na < K < Cs (i.e., the *opposite* of the order of hydration energies of the cations in bulk liquid water) [112]. In the second regime, from ½ to 1 ML, water uptake remains exothermic relative to bulk liquid water (by up to -10 kJ mol^{-1}) but becomes almost invariant with cation type. In the third regime, from 1 to 1½ ML, water uptake from bulk water is slightly exothermic on OH phlogopite but becomes slightly *endothermic* on F phlogopite (ΔH_{ads} = -1.0 ± 0.1, -0.1 ± 0.1, and -0.2 ± 0.1 kJ mol^{-1} on Na, K, and Cs OH phlogopite; 0.6 ± 0.1, 1.4 ± 0.2, and 0.8 ± 0.2 kJ mol^{-1} on Na, K, and Cs F phlogopite). Finally, at film thicknesses > 1½ ML (the fourth adsorption regime), water uptake from bulk liquid water is slightly exothermic in all systems (ΔH_{ads} = -0.94 ± 0.03, -0.52 ± 0.07, and -0.37 ± 0.07 kJ mol^{-1} on Na, K, and Cs OH phlogopite; -0.93 ± 0.03, -0.66 ± 0.05, and -0.48 ± 0.06 kJ mol^{-1} on Na, K, and Cs F phlogopite). In the last regime, the small yet statistically significant exothermic character of water uptake increases in the order of Cs < K < Na (i.e., in the same order as the hydration energies of the cations in bulk liquid water), indicating a transition towards bulk-liquid-water-like behavior. Our results further indicate that the energetics of water adsorption

remain distinctly influenced by the phlogopite surface even at film thickness of 3 ML or more. These distinct regimes in undersaturated conditions suggest that hygroscopic surfaces provided by minerals such as mica, as examined here, can significantly impact heterogeneous reactivity and photochemistry in conditions relevant to atmospheric sciences [5,113–116]. Finally, we note that the predicted trends in ΔH_{ads} vs. film thickness described above deviate from the only existing experimental dataset on the enthalpy of adsorption of water on mica (for the muscovite mica system), where a broad minimum in ΔH_{ads} was reported near 1 ML [39]. Our prediction of a minimum in ΔH_{ads} near 0 ML film thickness, however, is consistent with previous simulation results for mica [54] and with experimental and simulation results for other surfaces [42,117,118].

In line with the values of ΔH_{ads} presented above, our predicted values of ΔG_{ads} are most negative in the case of the dry surface and increase towards the value for bulk water (-26.7 kJ mol^{-1}, obtained in a separate simulation as described in Materials and Methods) with increasing film thickness. Results on ΔG_{ads} were not obtained at water coverages below 0.3 ML, where evaporation events were too infrequent to precisely quantify the average density of water vapor. At higher water coverages, error bars are too large to determine whether counterion type or structural F/OH groups impact ΔG_{ads}. Within the precision of the calculated values, however, our predicted ΔG_{ads} and ΔH_{ads} values show similar variations with film thickness, suggesting that the hygroscopic nature of phlogopite is determined primarily by the differential enthalpy of adsorption of water. A notable exception to this finding is presented by the adsorption of water to the surface of F phlogopite at 1 to 1½ ML coverage (the third adsorption regime), where an energetic barrier to water uptake (relative to pure bulk liquid water) is observed in ΔH_{ads} but not in ΔG_{ads}, suggesting that entropic effects facilitate the incipient formation of the second water monolayer. The corresponding predictions of water film thickness as a function of relative humidity (RH) yield identical trends for all systems within the precision of our results (Fig. 4c). Our results on RH vs. film thickness averaged across all six systems yield RH = 53 ± 9, 85 ± 7 and 97 ± 5% at water coverages of 1, 2, and 3 ML, respectively. Despite the non-negligible uncertainties, our simulation predictions are in excellent agreement with the experimental results of Cantrell and Ewing [39] and Balmer et al. [41] (shaded gray and green areas in Fig. 4c, respectively) at RH > 60%, where these two studies reported identical results. At RH < 60%, where the two experimental datasets diverge, our results match those of Balmer et al. [41]. Finally, at film thicknesses ≥ 2 ML, we also report in Fig. 4c a prediction of RH vs. film thickness, averaged across all six systems, estimated from the ΔH_{ads} values reported in Figs. 4a and 4b (i.e., a prediction that neglects the influence of entropy on the uptake of water from pure bulk liquid water to the adsorbed water film). Comparison of the gray and black circles in Fig. 4c reveals that the growth of > 2 ML thick adsorbed water films on mica in systems that contain pure bulk liquid water is driven by enthalpy and somewhat inhibited by entropic effects, suggesting that water molecules on the surface of the thin film have less configurational freedom than water molecules of the surface of pure liquid water.

Additional insight into the role of entropy is provided by our values of $-T\Delta S_{ads}$, calculated as the difference between ΔG_{ads} and ΔH_{ads} (Figs. 4a, b). Our results show that when the surface is only partially covered (< 0.9 ML), adsorption of water molecules is entropically disadvantageous relative to bulk liquid water, by 0.22 to 5 kJ mol^{-1}. This trend is particularly evident for the F phlogopite surface. Above 1 ML, $-T\Delta S_{ads}$ is close to the value for bulk liquid water in the case of OH phlogopite, whereas for F systems the entropic contribution shows a small yet significant dip at 1 to 1½ ML coverage suggesting an entropic favorability to transferring water from bulk liquid water to the adsorbed water film. In the next section, we examine the local coordination of water molecules and counterions to shed light on the structural basis of the trends in energetics identified here.

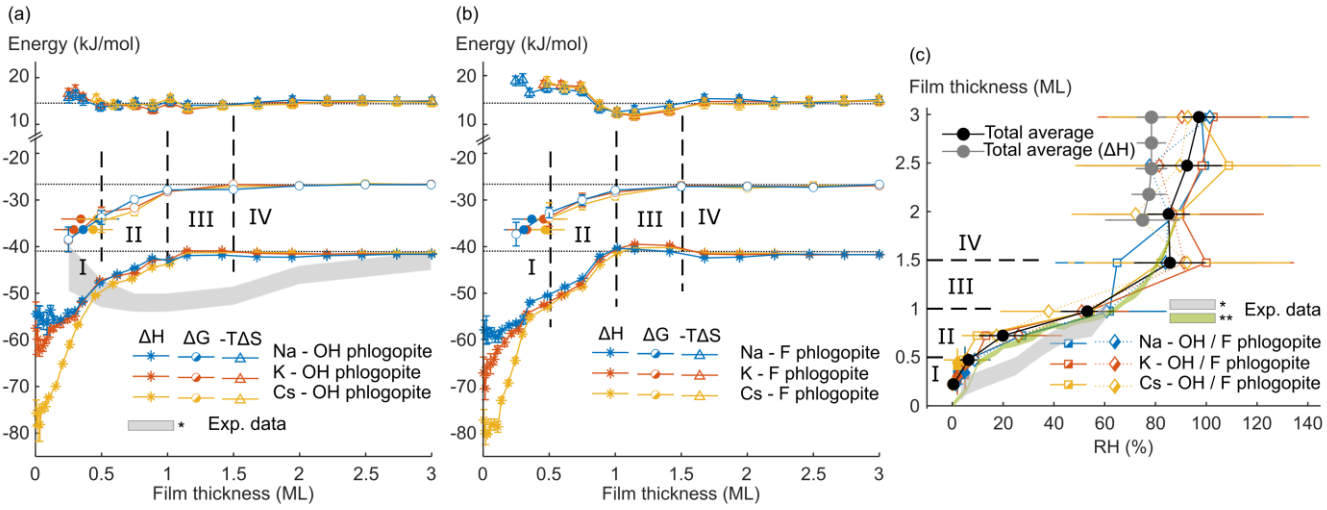

Figure 4. Energetics of water adsorption as a function of film thickness. (a, b) Differential free energy (ΔG_{ads}), and its enthalpic and entropic components (ΔH_{ads}, $-T\Delta S_{ads}$), associated with the addition of a single water molecule on Na-, K-, and Cs-bearing OH and F phlogopite surfaces with n-monolayer coverage ($0 < n \leq 3$). Horizontal dotted lines indicate values obtained for bulk liquid water using our MD simulation methodology (-26.68, -41.03, and 14.35 kJ mol^{-1}, respectively). Open and filled circles are free energies computed from MD or GCMC simulations, respectively. (c) Relationship between film thickness and relative humidity. Open and filled symbols (squares or diamonds) were obtained from MD or GCMC results, respectively. Filled black circles (with dashed line to guide the eye) show RH values averaged across the six systems with confidence intervals of two standard errors. Gray circles show analogous RH values averaged across all six systems derived from our ΔH_{ads} values for film thicknesses > 1.9 ML, based on the approximation that $-T\Delta S_{ads}$ is the same as in pure bulk

liquid water. Shaded areas in both (a) and (c) show experimental results reported by Cantrell and Ewing [39] (gray*) and Balmer et al. [41] (green**) for K-muscovite mica. Symbols I to IV refer to the four water adsorption regimes identified in the text.

Water Coordination in the Thin Film. The energetics presented in Fig. 4 suggest the existence of four distinct water adsorption regimes as a function of film thickness. These four regimes are examined below from the perspective of the molecular-level coordination of water (this section) and counterions (next section) in the thin film.

In Fig. 5, we present snapshots of the simulated systems for small portions of four representative surfaces (Na-F, Na-OH, K-OH, and Cs-OH phlogopite) at film thicknesses characteristic of the first adsorption regime (0.15 ML), where energetics presented above indicate that water adsorption is strongly influenced by the identity of the counterions. Snapshots of the entire surface are shown in Fig. S5. At this low coverage, water molecules are adsorbed mostly as single molecules or small clusters. A key feature that emerges from these snapshots is that Na ions strongly orient the water dipole moment away from the cation, whereas K and Cs ions do not, as also observed in studies of ions in bulk liquid water [119]. This orientational constraint of water molecules on Na-bearing surfaces inhibits the formation of hydrogen bonds between water molecules or with surface O atoms as illustrated, for example, by the existence of chains of hydrogen-bonded water molecules on Cs-mica but not on Na-mica in Fig. 5. This difference likely gives rise to the stronger hygroscopicity of Cs than K or Na-mica at < ½ ML water coverage.

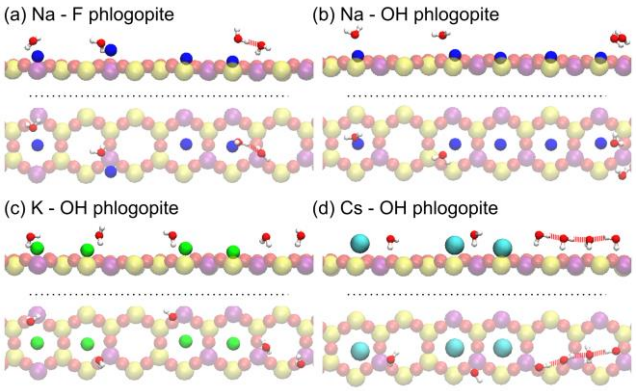

Figure 5. Snapshots of the adsorbed water film at 0.15 ML coverage on the surface of Na-F, Na-OH, K-OH, and Cs-OH phlogopite viewed from the side and the top. Hydrogen bonds are identified with an O···O distance cutoff of 3.5 Å and an OH-O···O angle cutoff of 30°. Larger-scale views are presented in Fig. S5.

Additional evidence of the phenomenon identified above is presented in Fig. 6, where the number of hydrogen bonds received per surface O atom is reported as a function of film thickness. Results are further broken down into the contribution from regular siloxane O atoms (Ob) vs. siloxane O atoms that coordinate an isomorphic substitution site (Obts). These two types of O atoms are equally abundant on the siloxane surface, but the Obts atoms carry about 11% more negative charge than Ob atoms on the CLAYFF model. At film thicknesses characteristic of the first adsorption regime, from 0 to ½ ML, Fig. 6 shows that adsorbed water molecules form significantly more hydrogen bonds with surface O atoms on Cs-bearing mica than on K- or Na-bearing mica (again suggesting greater orientational freedom of water molecules on Cs-mica) and that these bonds are predominantly donated to Obts. The strong sensitivity of water coordination (and of adsorption energetics) to the identity of the exchangeable cations is consistent with observations that the siloxane surface of smectite clay minerals (isostructural to that of mica) is inherently hydrophobic in the absence of counterions, i.e., surface hydrophobicity primarily stems from the adsorbed counterions [120,121]. A significant difference, however, is that most smectites carry predominantly Ob (and relatively few Obts) atoms on their basal surfaces due to their lower fraction of tetrahedral versus octahedral substitutions.

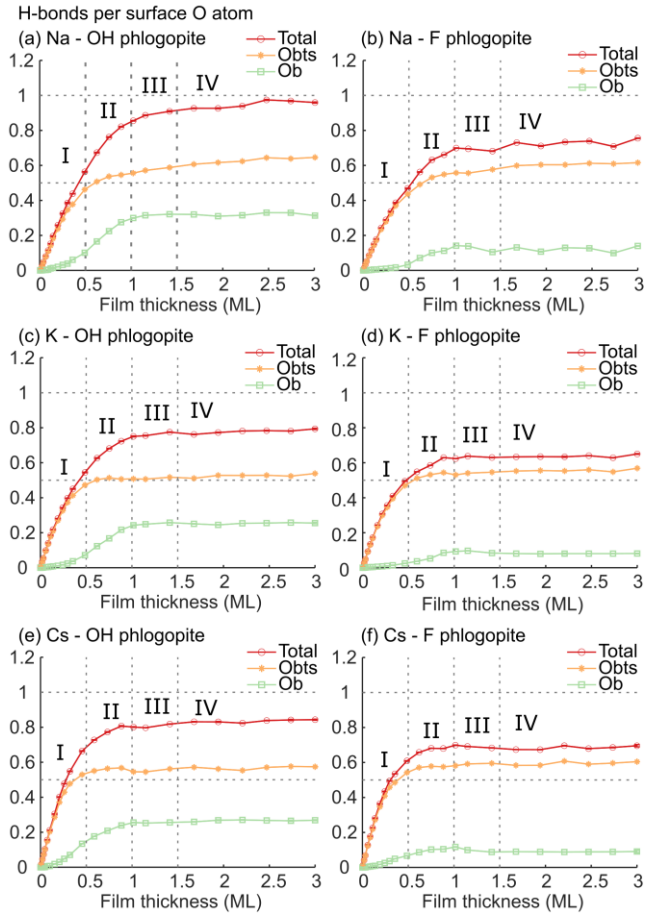

Figure 6. Number of hydrogen bonds formed per siloxane oxygen as a function of film thickness. Results are subdivided into the contributions of surface Ob and Obts atoms. The number of H-bonds reported here is evaluated approximately by integrating the radial distribution function between surface O and water O atoms to its first minimum. Symbols I to IV refer to the four water adsorption regimes identified in the text.

A second key feature that emerges from our observations of coordination structure in the water film is that water molecules adsorbed from 0 to ½ ML preferentially donate hydrogen bonds to siloxane O atoms located near isomorphic substitutions (Obts) whereas water molecules adsorbed from ½ to 1 ML (the second adsorption regime) preferentially donate hydrogen bonds to regular siloxane O atoms (Ob). The relative abundance of this latter type of hydrogen bond in the second adsorption regime is particularly sensitive to the identity of the adsorbed counterion (in the order Cs < K < Na) and to the degree of fluorination of the mica structure (in the order F < OH). Interestingly, the much greater tendency of Ob atoms on certain mica surfaces (notably, Na-OH mica) than on other mica surfaces (K- or Cs-

exchanged and/or fluorinated mica) to receive hydrogen bonds from water, established between ½ and 1 ML water coverage (the second adsorption regime), persists at higher water coverages as shown in Fig. 6. This phenomenon is further illustrated by the existence of persistently dehydrated patches on the surface of Na-F mica but not Na-OH mica at 1.2 ML water coverage, as demonstrated in Fig. 7.

Ion Coordination in the Thin Film. In Figure 8, we illustrate the local configuration of adsorbed cations and its change with increasing film thickness based on two measures: coordination number (CN) and bond-valence (BV), shown in the left and right columns, respectively. While the former simply describes the number of closest neighbors, here corresponding to water oxygens (Ow) and surface siloxane oxygens (Ob and Obts), the latter is a semi-empirical measure of coordination 'strength' obtained by assigning higher strength to shorter-ranged interactions, as described in Materials and Methods. One notable feature in the former representation is that the CN values for K and Cs are practically invariant with film thickness above 1 ML, whereas the CN values for Na continue to vary with film thickness up to at least 3 ML. This is consistent with the progressive growth of the IS2 and OS peaks with increasing film thickness up to at least 3 ML in the Na systems (Fig. 2a), i.e., with the formation of an incipient electrical double layer on Na mica. We also note that in the K and Cs systems, as film thickness increases from 0 to 1 ML, the BV shared by the cation with surface O atoms decreases even though the CN is constant. This implies that the cations maintain the same overall configuration but move away from the surface, in agreement with our observations based on Fig. 2.

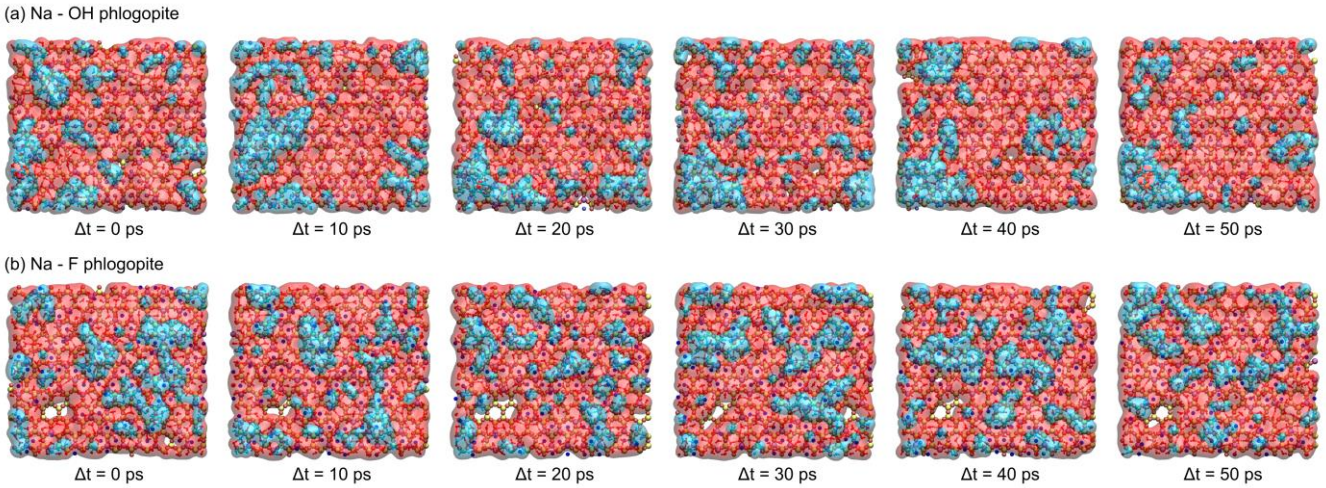

Figure 7. Top-view snapshots of the adsorbed water film at 10 ps intervals on the surface of (a) Na-OH and (b) Na-F phlogopite at a film thickness of 1.2 ML. First and second adsorbed water monolayers are displayed as three-dimensional surfaces in pink and cyan, respectively. The figure shows the existence of persistent dewetted spots (where ditrigonal cavities can be seen) on the Na-F surface.

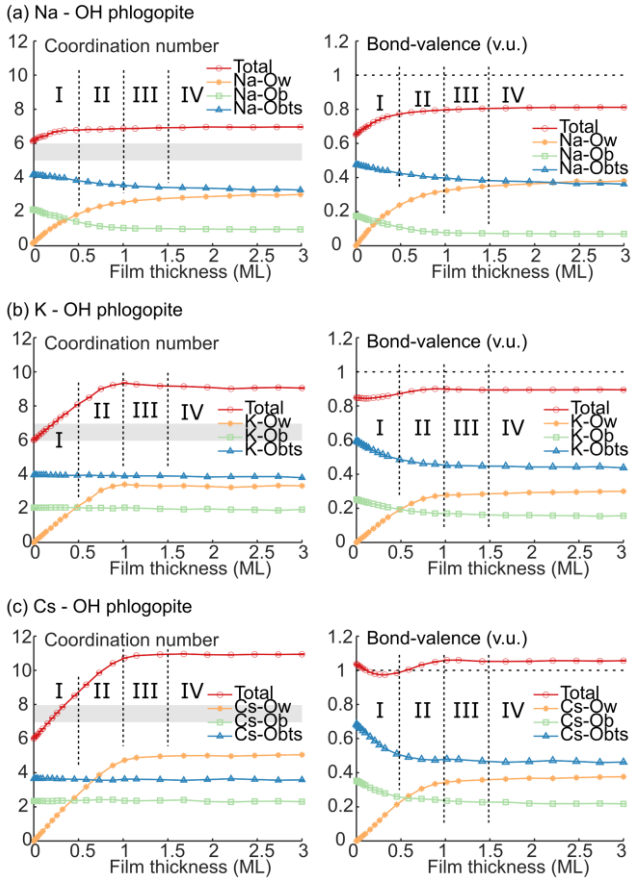

Figure 8. Two measures of surface counterion local configuration on (a) Na-, (b) K-, and (c) Cs-OH phlogopite. Coordination number (CN, left column) and bond valence (BV, right column) for respective counterions with respect to water oxygen (Ow), surface bridging oxygens (Ob), and surface bridging oxygens with isomorphic substitutions (Obts) as a function of film thickness. Shaded areas (left) indicate hydration numbers reported in the literature and horizontal dotted lines (right) indicate the expected BV sum for monovalent cations (+1). Symbols I to IV refer to the four water adsorption regimes identified in the text.

CONCLUSIONS

This study addresses the challenge associated with detailed characterization of thin adsorbed water films and mechanistic understanding of their stability using atomistic simulations complemented by experimental determination of the interfacial structure using in situ XRR. We modulate two variables that are expected to impact surface hygroscopicity (adsorbed counterions and structural F/OH composition) and examine the resulting impacts on the process of surface hydration as a function of film thickness from a perspective of single water molecules to clusters and thin films. We find that, while the basal surface of mica minerals is generally considered highly hydrophilic, adsorption energetics and local coordination in the thin film differ significantly between the different mica surfaces, especially when the surfaces are unsaturated. More specifically, we identify four distinct regimes of surface hydration. The first regime, corresponding to film thickness below ½ ML, is highly sensitive to counterion type and is characterized by ΔH values that become more negative in the order of Na < K < Cs (opposite of the order of the hydration enthalpy of the ions in bulk liquid water). This suggests that Cs-mica is more hygroscopic than K- and Na-micas in this regime and is consistent with the increasing height of the first water density peaks at 0.3 ML in the order Na < K < Cs. The second regime, corresponding to film thickness from ½ to 1 ML, is mainly controlled by the hydration of the uncharged regions of the siloxane surface. While the adsorption energetics for different surfaces show little difference, water clusters exhibit distinct local configurations depending on exchangeable cation type and structural fluorination. In particular, water clusters on Na-mica show a greater tendency to coat the entire surface as compared with K- or Cs-mica. The third regime, corresponding to film thickness from ~1 to 1½ ML, entails an enthalpic barrier for fluorinated systems. Our results in this regime also show evidence of persistently dewetted patches, particularly on F-phlogopite surfaces, that may serve as preferential sites for hydrophobic adsorption and heterogeneous nucleation of non-aqueous phases despite the overall hygroscopic nature of the mica surface. The final regime above 1½ ML is characterized by the formation of an incipient electrical double layer at the mineral-water interface, particularly in the case of Na-OH phlogopite, such that water adsorption remains energetically more favorable with respect to the bulk liquid water surface up to film thickness of at least 3 ML. In this last regime, hygroscopicity increases in the order Cs < K< Na, the opposite of the order observed at low water coverage, reflecting the transition from isolated water molecules (below ½ ML) to a collective water network (above 1½ ML) combined with the tendency of different ions to enhance (in the case of Na) or inhibit (in the case of Cs) the cooperativity of the water hydrogen-bond network. These results show that the hygroscopicity of natural mineral surfaces has a complex dependence on film thickness, counterions type, structural fluorination, and their spatial location on the surface.

ASSOCIATED CONTENT

Supporting Information

The Supporting Information is available free of charge on the ACS Publications website. It includes simulation details of the hybrid GCMC+MD technique; additional details of the XRR data analysis; supporting figures showing density profiles, adsorption energetics, and MD simulation snapshots, as well as an excel file containing differential electron density data.

AUTHOR INFORMATION

Corresponding Author

*Corresponding author: akoishi@lbl.gov; sslee@anl.gov

Present Addresses

#A.K.: Energy Geosciences Division, Lawrence Berkeley National Laboratory, 1 Cyclotron Road, Berkeley, CA 94720, United States

Author Contributions

AK, AFM, ICB designed research; AK performed simulations; AK, SSL performed experiments; and AK, SSL, PF, ICB wrote the manuscript.

ACKNOWLEDGMENT

This work was supported by the U.S. Department of Energy, Office of Science, Office of Basic Energy Sciences, Geosciences Program under Award DE-SC0018419 to Princeton University (AK and ICB for computational simulations, experimental data collection, and analyses) and Contract DE-AC02-06CH11357 to UChicago

Argonne, LLC as operator of Argonne National Laboratory (SSL and PF for measurements and analyses of XRR data). Molecular dynamics simulations were carried out using resources of the National Energy Research Scientific Computing Center (NERSC), which is supported by the U.S. Department of Energy, Office of Science, under award DE-AC02-05CH11231. APS (33-ID-D) and Diamond (I19-1) facilities are acknowledged for beamtime allocation. Use of APS was supported by the U.S. Department of Energy, Office of Science, Office of Basic Energy Sciences. AK acknowledges Phil Jeffrey for single crystal X-ray diffraction data refinement. The U.S. Government retains for itself, and others acting on its behalf, a paid-up nonexclusive, irrevocable worldwide license in said article to reproduce, prepare derivative works, distribute copies to the public, and perform publicly and display publicly, by or on behalf of the Government.

REFERENCES

(1) Shahraeeni, E.; Or, D. Pore-Scale Analysis of Evaporation and Condensation Dynamics in Porous Media. *Langmuir* **2010**, *26*, 13924–13936.

(2) Lebeau, M.; Konrad, J. M. A New Capillary and Thin Film Flow Model for Predicting the Hydraulic Conductivity of Unsaturated Porous Media. *Water Resour. Res.* **2010**, *46*, 1–15.

(3) Wan, J.; Tokunaga, T. K. Film Straining of Colloids in Unsaturated Porous Media: Conceptual Model and Experimental Testing. *Environ. Sci. Technol.* **1997**, *31*, 2413–2420.

(4) Hu, Q.; Kneafsey, T. J.; Roberts, J. J.; Tomutsa, L.; Wang, J. S. Y. Characterizing Unsaturated Diffusion in Porous Tuff Gravel. *Vadose Zo. J.* **2004**, *3*, 1425–1438.

(5) Tang, M.; Cziczo, D. J.; Grassian, V. H. Interactions of Water with Mineral Dust Aerosol: Water Adsorption, Hygroscopicity, Cloud Condensation, and Ice Nucleation. *Chem. Rev.* **2016**, *116*, 4205–4259.

(6) Yeşilbaş, M.; Boily, J. F. Particle Size Controls on Water Adsorption and Condensation Regimes at Mineral Surfaces. *Sci. Rep.* **2016**, *6*, 1–10.

(7) Yeşilbaş, M.; Boily, J. F. Thin Ice Films at Mineral Surfaces. *J. Phys. Chem. Lett.* **2016**, *7*, 2849–2855.

(8) Yalcin, S. E.; Legg, B. A.; Yeşilbaş, M.; Malvankar, N. S.; Boily, J. F. Direct Observation of Anisotropic Growth of Water Films on Minerals Driven by Defects and Surface Tension. *Sci. Adv.* **2020**, *6*, 1–10.

(9) Espinoza, D. N.; Santamarina, J. C. Water-CO2-mineral Systems: Interfacial Tension, Contact Angle, and Diffusion—Implications to CO2 Geological Storage. *Water Resour. Res.* **2010**, *46*.

(10) Placencia-Gómez, E.; Kerisit, S. N.; Mehta, H. S.; Qafoku, O.; Thompson, C. J.; Graham, T. R.; Ilton, E. S.; Loring, J. S. Critical Water Coverage during Forsterite Carbonation in Thin Water Films: Activating Dissolution and Mass Transport. *Environ. Sci. Technol.* **2020**, *54*, 6888–6899.

(11) Churakov, S. V. Mobility of Na and Cs on Montmorillonite Surface under Partially Saturated Conditions. *Environ. Sci. Technol.* **2013**, *47*, 9816–9823.

(12) Mugele, F.; Baret, J. C. Electrowetting: From Basics to Applications. *J. Phys. Condens. Matter* **2005**, *17*.

(13) Boo, C.; Hong, S.; Elimelech, M. Relating Organic Fouling in Membrane Distillation to Intermolecular Adhesion Forces and Interfacial Surface Energies. *Environ. Sci. Technol.* **2018**, *52*, 14198–14207.

(14) Jamadagni, S. N.; Godawat, R.; Garde, S. Hydrophobicity of Proteins and Interfaces: Insights from Density Fluctuations. *Annu. Rev. Chem. Biomol. Eng.* **2011**, *2*, 147–171.

(15) Speer, S. L.; Zheng, W.; Jiang, X.; Chu, I. Te; Guseman, A. J.; Liu, M.; Pielak, G. J.; Li, C. The Intracellular Environment Affects Protein-Protein Interactions. *Proc. Natl. Acad. Sci. U. S. A.* **2021**, *118*, 1–7.

(16) Iskrenova-Tchoukova, E.; Kalinichev, A. G.; Kirkpatrick, R. J. Metal Cation Complexation with Natural Organic Matter in Aqueous Solutions: Molecular Dynamics Simulations and Potentials of Mean Force. *Langmuir* **2010**, *26*, 15909–15919.

(17) Dor, M.; Levi-Kalisman, Y.; Day-Stirrat, R. J.; Mishael, Y.; Emmanuel, S. Assembly of Clay Mineral Platelets, Tactoids, and Aggregates: Effect of Mineral Structure and Solution Salinity. *J. Colloid Interface Sci.* **2020**, *566*, 163–170.

(18) Shen, X.; Bourg, I. C. Molecular Dynamics Simulations of the Colloidal Interaction between Smectite Clay Nanoparticles in Liquid Water. *J. Colloid Interface Sci.* **2020**, *584*, 610–621.

(19) Gianti, E.; Delemotte, L.; Klein, M. L.; Carnevale, V. On the Role of Water Density Fluctuations in the Inhibition of a Proton Channel. *Proc. Natl. Acad. Sci. U. S. A.* **2016**, *113*, E8359–E8368.

(20) Zachara, J.; Brantley, S.; Chorover, J.; Ewing, R.; Kerisit, S.; Liu, C.; Perfect, E.; Rother, G.; Stack, A. G. Internal Domains of Natural Porous Media Revealed: Critical Locations for Transport, Storage, and Chemical Reaction. *Environ. Sci. Technol.* **2016**, *50*, 2811–2829.

(21) Kim, M.; Or, D. Microscale PH Variations during Drying of Soils and Desert Biocrusts Affect HONO and NH3 Emissions. *Nat. Commun.* **2019**, *10*, 1–12.

(22) Miranda, P. B.; Xu, L.; Shen, Y. R.; Salmeron, M. Icelike Water Monolayer Adsorbed on Mica at Room Temperature. *Phys. Rev. Lett.* **1998**, *81*, 5876–5879.

(23) Odelius, M.; Bernasconi, M.; Parrinello, M. Two Dimensional Ice Adsorbed on Mica Surface. *Phys. Rev. Lett.* **1997**, *78*, 2855–2858.

(24) French, R. H.; Parsegian, V. A.; Podgornik, R.; Rajter, R. F.; Jagota, A.; Luo, J.; Asthagiri, D.; Chaudhury, M. K.; Chiang, Y.; Granick, S.; et al. Long Range Interactions in Nanoscale Science. *Rev. Mod. Phys.* **2010**, *82*, 1887–1944.

(25) Langmuir, I. Repulsive Forces between Charged Surfaces in Water, and the Cause of the Jones-Ray Effect. *Science* **1938**, *88*, 430–432.

(26) Siretanu, I.; Ebeling, D.; Andersson, M. P.; Stipp, S. L. S.; Philipse, A.; Stuart, M. C.; van den Ende, D.; Mugele, F. Direct Observation of Ionic Structure at Solid-Liquid Interfaces: A Deep Look into the Stern Layer. *Sci. Rep.* **2014**, *4*.

(27) Van Lin, S. R.; Grotz, K. K.; Siretanu, I.; Schwierz, N.; Mugele, F. Ion-Specific and PH-Dependent Hydration of Mica-Electrolyte Interfaces. *Langmuir* **2019**, *35*, 5737–5745.

(28) Bourg, I. C.; Lee, S. S.; Fenter, P.; Tournassat, C. Stern Layer Structure and Energetics at Mica-Water Interfaces. *J. Phys. Chem. C* **2017**, *121*, 9402–9412.

(29) Fenter, P.; Lee, S. S. Hydration Layer Structure at Solid–Water Interfaces. *MRS Bull.* **2014**, *39*, 1056–1061.

(30) Eng, P. J.; Trainor, T. P.; Brown Jr., G. E.; Waychunas, G. A.; Newville, M.; Sutton, S. R.; Rivers, M. L. Structure of the Hydrated α-Al2O3 (0001) Surface. *Science* **2000**, *288*, 1029–1033.

(31) Al-Abadleh, H. A.; Grassian, V. H. FT-IR Study of Water Adsorption on Aluminum Oxide Surfaces. *Langmuir* **2003**, *19*, 341–347.

(32) Arsic, J.; Kaminski, D. M.; Radenovic, N.; Poodt, P.; Graswinckel, W. S.; Cuppen, H. M.; Vlieg, E. Thickness-Dependent Ordering of Water Layers at the NaCl(100) Surface. *J. Chem. Phys.* **2004**, *120*, 9720–9724.

(33) Fenter, P.; Lee, S. S.; Zhang, Z.; Sturchio, N. C. In Situ Imaging of Orthoclase-Aqueous Solution Interfaces with x-Ray Reflection Interface Microscopy. *J. Appl. Phys.* **2011**, *110*.

(34) Ruta, B.; Zontone, F.; Chushkin, Y.; Baldi, G.; Pintori, G.; Monaco, G.; Rufflé, B.; Kob, W. Hard X-Rays as Pump and Probe of Atomic Motion in Oxide Glasses. *Sci. Rep.* **2017**, *7*, 3962.

(35) Laanait, N.; Callagon, E. B. R.; Zhang, Z.; Sturchio, N. C.; Lee, S. S.; Fenter, P. X-Ray-Driven Reaction Front Dynamics at Calcite-Water Interfaces. *Science* **2015**, *349*, 1330–1334.

(36) Hu, J.; Xiao, X. d.; Ogletree, D. F.; Salmeron, M. The Structure of Molecularly Thin Films of Water on Mica in Humid Environments. *Surf. Sci.* **1995**, *344*, 221–236.

(37) Santos, S.; Verdaguer, A.; Souier, T.; Thomson, N. H.; Chiesa, M. Measuring the True Height of Water Films on Surfaces. *Nanotechnology* **2011**, *22*.

(38) Santos, S.; Verdaguer, A. Imaging Water Thin Films in Ambient Conditions Using Atomic Force Microscopy. *Materials (Basel).* **2016**, *9*, 1–16.

(39) Cantrell, W.; Ewing, G. E. Thin Film Water on Muscovite Mica. *J. Phys. Chem. B* **2001**, *105*, 5434–5439.

(40) Rakhmatkariev, G. Mechanism of Adsorption of Water Vapor by Muscovite: A Model Based on Adsorption Calorimetry. *Clays Clay Miner.* **2006**, *54*, 402–407.

(41) Balmer, T. E.; Christenson, H. K.; Spencer, N. D.; Heuberger, M.

The Effect of Surface Ions on Water Adsorption to Mica. *Langmuir* **2008**, *24*, 1566–1569.

(42) Majzlan, J.; Mazeina, L.; Navrotsky, A. Enthalpy of Water Adsorption and Surface Enthalpy of Lepidocrocite (γ-FeOOH). *Geochim. Cosmochim. Acta* **2007**, *71*, 615–623.

(43) Guo, X.; Wu, D.; Ushakov, S. V.; Shvareva, T.; Xu, H.; Navrotsky, A. Energetics of Hydration on Uranium Oxide and Peroxide Surfaces. *J. Mater. Res.* **2019**, *34*, 3319–3325.

(44) Beaglehole, D.; Christenson, H. K. Vapor Adsorption on Mica and Silicon: Entropy Effects, Layering, and Surface Forces. *J. Phys. Chem.* **1992**, *96*, 3395–3403.

(45) Yamamoto, S.; Bluhm, H.; Andersson, K.; Ketteler, G.; Ogasawara, H.; Salmeron, M.; Nilsson, A. In Situ X-Ray Photoelectron Spectroscopy Studies of Water on Metals and Oxides at Ambient Conditions. *J. Phys. Condens. Matter* **2008**, *20*, 184025.

(46) Salmeron, M.; Schlögl, R. Ambient Pressure Photoelectron Spectroscopy: A New Tool for Surface Science and Nanotechnology. *Surf. Sci. Rep.* **2008**, *63*, 169–199.

(47) Tong, Y.; Kampfrath, T.; Campen, R. K. Experimentally Probing the Libration of Interfacial Water: The Rotational Potential of Water Is Stiffer at the Air/Water Interface than in Bulk Liquid. *Phys. Chem. Chem. Phys.* **2016**, *18*, 18424–18430.

(48) Boily, J. F.; Fu, L.; Tuladhar, A.; Lu, Z.; Legg, B. A.; Wang, Z. M.; Wang, H. Hydrogen Bonding and Molecular Orientations across Thin Water Films on Sapphire. *J. Colloid Interface Sci.* **2019**, *555*, 810–817.

(49) Arai, T.; Sato, K.; Iida, A.; Tomitori, M. Quasi-Stabilized Hydration Layers on Muscovite Mica under a Thin Water Film Grown from Humid Air. *Sci. Rep.* **2017**, *7*, 1–11.

(50) Rotenberg, B.; Patel, A. J.; Chandler, D. Molecular Explanation for Why Talc Surfaces Can Be Both Hydrophilic and Hydrophobic. *J. Am. Chem. Soc.* **2011**, *133*, 20521–20527.

(51) Tunega, D.; Gerzabek, M. H.; Lischka, H. Ab Initio Molecular Dynamics Study of a Monomolecular Water Layer on Octahedral and Tetrahedral Kaolinite Surfaces. *J. Phys. Chem. B* **2004**, *108*, 5930–5936.

(52) Meng, S.; Wang, E. G.; Gao, S. Water Adsorption on Metal Surfaces: A General Picture from Density Functional Theory Studies. *Phys. Rev. B - Condens. Matter Mater. Phys.* **2004**, *69*, 1–13.

(53) Chen, J.; Long, X.; Chen, Y. Comparison of Multilayer Water Adsorption on the Hydrophobic Galena (PbS) and Hydrophilic Pyrite (FeS2) Surfaces: A DFT Study. *J. Phys. Chem. C* **2014**, *118*, 11657–11665.

(54) Wang, J.; Kalinichev, A. G.; Kirkpatrick, R. J. Effects of Substrate Structure and Composition on the Structure, Dynamics, and Energetics of Water at Mineral Surfaces: A Molecular Dynamics Modeling Study. *Geochim. Cosmochim. Acta* **2006**, *70*, 562–582.

(55) Fernandez-Martinez, A.; Tao, J.; Wallace, A. F.; Bourg, I. C.; Johnson, M. R.; De Yoreo, J. J.; Sposito, G.; Cuello, G. J.; Charlet, L. Curvature-Induced Hydrophobicity at Imogolite-Water Interfaces. *Environ. Sci. Nano* **2020**, *7*, 2759–2772.

(56) Adapa, S.; Swamy, D. R.; Kancharla, S.; Pradhan, S.; Malani, A. Role of Mono- and Divalent Surface Cations on the Structure and Adsorption Behavior of Water on Mica Surface. *Langmuir* **2018**, *34*, 14472–14488.

(57) Kerisit, S.; Weare, J. H.; Felmy, A. R. Structure and Dynamics of Forsterite-ScCO 2/H 2O Interfaces as a Function of Water Content. *Geochim. Cosmochim. Acta* **2012**, *84*, 137–151.

(58) Malani, A.; Ayappa, K. G. Adsorption Isotherms of Water on Mica: Redistribution and Film Growth. *J. Phys. Chem. B* **2009**, *113*, 1058–1067.

(59) Phan, A.; Ho, T. A.; Cole, D. R.; Striolo, A. Molecular Structure and Dynamics in Thin Water Films at Metal Oxide Surfaces: Magnesium, Aluminum, and Silicon Oxide Surfaces. *J. Phys. Chem. C* **2012**, *116*, 15962–15973.

(60) Ou, X.; Wang, X.; Lin, Z.; Li, J. Heterogeneous Condensation of Water on the Mica (001) Surface: A Molecular Dynamics Simulation Work. *J. Phys. Chem. C* **2017**, *121*, 6813–6819.

(61) Zhao, G.; Tan, Q.; Xiang, L.; Cai, D.; Zeng, H.; Yi, H.; Ni, Z.; Chen, Y. Structure and Properties of Water Film Adsorbed on Mica Surfaces. *J. Chem. Phys.* **2015**, *143*.

(62) Ketteler, G.; Yamamoto, S.; Bluhm, H.; Andersson, K.; Starr, D. E.; Ogletree, D. F.; Ogasawara, H.; Nilsson, A.; Salmeron, M. The Nature of Water Nucleation Sites on TiO 2 (110) Surfaces Revealed by Ambient Pressure X-Ray Photoelectron Spectroscopy. *J. Phys. Chem. C* **2007**, *111*, 8278–8282.

(63) Ma, S. Y.; Liu, L. M.; Wang, S. Q. Water Film Adsorbed on the α-Al2O3(0001) Surface: Structural Properties and Dynamical Behaviors from First-Principles Molecular Dynamics Simulations. *J. Phys. Chem. C* **2016**, *120*, 5398–5409.

(64) Newberg, J. T.; Starr, D. E.; Yamamoto, S.; Kaya, S.; Kendelewicz, T.; Mysak, E. R.; Porsgaard, S.; Salmeron, M. B.; Brown, G. E.; Nilsson, A.; et al. Formation of Hydroxyl and Water Layers on MgO Films Studied with Ambient Pressure XPS. *Surf. Sci.* **2011**, *605*, 89–94.

(65) Yamamoto, S.; Kendelewicz, T.; Newberg, J. T.; Ketteler, G.; Starr, D. E.; Mysak, E. R.; Andersson, K. J.; Ogasawara, H.; Bluhm, H.; Salmeron, M.; et al. Water Adsorption on α-Fe_2O_3(0001) at near Ambient Conditions. *J. Phys. Chem. C* **2010**, *114*, 2256–2266.

(66) Sposito, G.; Skipper, N. T.; Sutton, R.; Park, S. H.; Soper, A. K.; Greathouse, J. A. Surface Geochemistry of the Clay Minerals. *Proc. Natl. Acad. Sci. U. S. A.* **1999**, *96*, 3358–3364.

(67) Sposito, G.; Prost, R. Structure of Water Adsorbed on Smectites. *Chem. Rev.* **1982**, *82*, 553–573.

(68) Kobayashi, K.; Liang, Y.; Amano, K. I.; Murata, S.; Matsuoka, T.; Takahashi, S.; Nishi, N.; Sakka, T. Molecular Dynamics Simulation of Atomic Force Microscopy at the Water-Muscovite Interface: Hydration Layer Structure and Force Analysis. *Langmuir* **2016**, *32*, 3608–3616.

(69) Fukuma, T.; Ueda, Y.; Yoshioka, S.; Asakawa, H. Atomic-Scale Distribution of Water Molecules at the Mica-Water Interface Visualized by Three-Dimensional Scanning Force Microscopy. *Phys. Rev. Lett.* **2010**, *104*, 2–5.

(70) Stubbs, J. E.; Legg, B. A.; Lee, S. S.; Dera, P.; De Yoreo, J. J.; Fenter, P.; Eng, P. J. Epitaxial Growth of Gibbsite Sheets on the Basal Surface of Muscovite Mica. *J. Phys. Chem. C* **2019**.

(71) Alcantar, N.; Israelachvili, J.; Boles, J. Forces and Ionic Transport between Mica Surfaces: Implications for Pressure Solution. *Geochim. Cosmochim. Acta* **2003**, *67*, 1289–1304.

(72) Kuwahara, Y. Comparison of the Surface Structure of the Tetrahedral Sheets of Muscovite and Phlogopite by AFM. *Phys. Chem. Miner.* **2001**, *28*.

(73) Bailey, S. W. Crystal Chemistry of the True Micas. In *Micas*; Bailey, S. W., Ed.; Mineralogical Society of America, 1984; pp 13–60.

(74) Petersen, E. U.; Essene, E. J.; Peacor, D. R.; Valley, J. W. Fluorine End-Member Micas and Amphiboles. *Am. Mineral.* **1982**, *67*, 538–544.

(75) *Handbook of Geochemistry: Vol. II/1*; Wedepohl, K. H., Ed.; Springer-Verlag, 1978.

(76) Dazas, B.; Lanson, B.; Breu, J.; Robert, J. L.; Pelletier, M.; Ferrage, E. Smectite Fluorination and Its Impact on Interlayer Water Content and Structure: A Way to Fine Tune the Hydrophilicity of Clay Surfaces? *Microporous Mesoporous Mater.* **2013**, *181*, 233–247.

(77) Michot, L. J.; Villieras, F.; Francois, M.; Yvon, J.; Le Dred, R.; Cases, J. M. The Structural Microscopic Hydrophilicity of Talc. *Langmuir* **1994**, *10*, 3765–3773.

(78) Valley, J. W.; Petersen, E. U.; Essene, E. J.; Bowman, J. R. Fluorphlogopite and Fluortremolite in Adirondack Marbles and Calculated C-O-H-F Fluid Compositions. *Am. Mineral.* **1982**, *67*, 545–557.

(79) Kearns, L. E.; Kite, L. E.; Leavens, P. B.; Nelen, J. A. Fluorine Distribution in the Hydrous Silicate Minerals of the Franklin Marble, Orange County, New York. *Fluor. Distrib. hydrous Silic. Miner. Franklin Marble, Orange County, New York* **1980**, *65*, 557–562.

(80) Li, Y.; Jiang, H.; Yang, X. Fluorine Follows Water: Effect on Electrical Conductivity of Silicate Minerals by Experimental Constraints from Phlogopite. *Geochim. Cosmochim. Acta* **2017**, *217*, 16–27.

(81) Ryckaert, J. P. J.; Ciccotti, G.; Berendsen, H. J. C. J. Numerical Integration of the Cartesian Equations of Motion of a System with Constraints: Molecular Dynamics of n-Alkanes. *J. Comput. Phys.* **1977**, *23*, 327–341.

(82) Berendsen, H. J. C.; Postma, J. P. M.; van Gunsteren, W. F.;

Herman, J. Interaction Models for Water in Relation to Protein Hydration. In *Intermolecular Forces*; 1981; pp 331–342.
(83) Cygan, R. T.; Liang, J.-J. J.; Kalinichev, A. G. Molecular Models of Hydroxide, Oxyhydroxide, and Clay Phases and the Development of a General Force Field. *J. Phys. Chem. B* **2004**, *108*, 1255–1266.
(84) Dang, L. X. Mechanism and Thermodynamics of Ion Selectivity in Aqueous Solutions of 18-Crown-6 Ether: A Molecular Dynamics Study. *J. Am. Chem. Soc.* **1995**, *117*, 6954–6960.
(85) Marry, V.; Dubois, E.; Malikova, N.; Durand-Vidal, S.; Longeville, S.; Breu, J. Water Dynamics in Hectorite Clays: Infuence of Temperature Studied by Coupling Neutron Spin Echo and Molecular Dynamics. *Environ. Sci. Technol.* **2011**, *45*, 2850–2855.
(86) Dang, L. X. Fluoride-Fluoride Association in Water from Molecular Dynamics Simulations. *Chem. Phys. Lett.* **1992**, *200*, 21–25.
(87) Ferrage, E.; Sakharov, B. A.; Michot, L. J.; Delville, A.; Bauer, A.; Lanson, B.; Grangeon, S.; Frapper, G.; Jiménez-Ruiz, M.; Cuello, G. J. Hydration Properties and Interlayer Organization of Water and Ions in Synthetic Na-Smectite with Tetrahedral Layer Charge. Part 2. Toward a Precise Coupling between Molecular Simulations and Diffraction Data. *J. Phys. Chem. C* **2011**, *115*, 1867–1881.
(88) Holmboe, M.; Bourg, I. C. Molecular Dynamics Simulations of Water and Sodium Diffusion in Smectite Interlayer Nanopores as a Function of Pore Size and Temperature. *J. Phys. Chem. C* **2014**, *118*, 1001–1013.
(89) Boulougouris, G. C.; Economou, I. G.; Theodorou, D. N. Engineering a Molecular Model for Water Phase Equilibrium over a Wide Temperature Range. *J. Phys. Chem. B* **2002**, *102*, 1029–1035.
(90) Vorholz, J.; Harismiadis, V. I.; Rumpf, B.; Panagiotopoulos, A. Z.; Maurer, G. Vapor+liquid Equilibrium of Water, Carbon Dioxide, and the Binary System, Water+carbon Dioxide, from Molecular Simulation. *Fluid Phase Equilib.* **2000**, *170*, 203–234.
(91) Plimpton, S. Fast Parallel Algorithms for Short-Range Molecular Dynamics. *Journal of Computational Physics*. 1995, pp 1–19.
(92) I. D. Brown. Bond Valence Theory. In *Structure and Bonding*; 2006; Vol. 119, pp 193–223.
(93) Brown, I. D.; Altermatt, D. Bond-Valence Parameters Obtained from a Systematic Analysis of the Inorganic Crystal Structure Database. *Acta Crystallogr.* **1985**, *244*, 244–247.
(94) Bickmore, B. R.; Rosso, K. M.; Brown, I.; Kerisit, S. Bond-Valence Constraints on Liquid Water Structure. *J. Phys. Chem. A* **2009**, *113*, 1847–1857.
(95) Fenter, P.; Lee, S. S.; Skelton, A. A.; Cummings, P. T. Direct and Quantitative Comparison of Pixelated Density Profiles with High-Resolution X-Ray Reflectivity Data. *J. Synchrotron Radiat.* **2011**, *18*, 257–265.
(96) Lee, S. S.; Fenter, P.; Nagy, K. L.; Sturchio, N. C. Monovalent Ion Adsorption at the Muscovite (001)-Solution Interface: Relationships among Ion Coverage and Speciation, Interfacial Water Structure, and Substrate Relaxation. *Langmuir* **2012**, *28*, 8637–8650.
(97) Wang, J.; Kalinichev, A. G.; Kirkpatrick, R. J.; Cygan, R. T. Structure, Energetics, and Dynamics of Water Adsorbed on the Muscovite (001) Surface: A Molecular Dynamics Simulation. *J. Phys. Chem. B* **2005**, *109*, 15893–15905.
(98) Cheng, L.; Fenter, P.; Nagy, K. L.; Schlegel, M. L.; Sturchio, N. C. Molecular-Scale Density Oscillations in Water Adjacent to a Mica Surface. *Phys. Rev. Lett.* **2001**, *87*, 156103.
(99) Park, S.-H.; Sposito, G. Structure of Water Adsorbed on a Mica Surface. *Phys. Rev. Lett.* **2002**, *89*, 085501.
(100) Schlegel, M. L.; Nagy, K. L.; Fenter, P.; Cheng, L.; Sturchio, N. C.; Jacobsen, S. D. Cation Sorption on the Muscovite (0 0 1) Surface in Chloride Solutions Using High-Resolution X-Ray Reflectivity. *Geochim. Cosmochim. Acta* **2006**, *70*, 3549–3565.
(101) Israelachvili, J. N.; Pashley, R. M. Molecular Layering of Water at Surfaces and Origin of Repulsive Hydration Forces. *Nature*. 1983, pp 249–250.
(102) Bourg, I. C.; Sposito, G. Molecular Dynamics Simulations of the Electrical Double Layer on Smectite Surfaces Contacting Concentrated Mixed Electrolyte (NaCl-CaCl2) Solutions. *J. Colloid Interface Sci.* **2011**, *360*, 701–715.
(103) Fumagalli, L.; Esfandiar, A.; Fabregas, R.; Hu, S.; Ares, P.; Janardanan, A.; Yang, Q.; Radha, B.; Taniguchi, T.; Watanabe, K.; et al. Anomalously Low Dielectric Constant of Confined Water Downloaded From. *Science* **2018**, *360*, 1339–1342.
(104) Fayer, M. D. Dynamics of Water Interacting with Interfaces, Molecules, and Ions. *Acc. Chem. Res.* **2012**, *45*, 3–14.
(105) Loh, S. H.; Jarvis, S. P. Visualization of Ion Distribution at the Mica-Electrolyte Interface. *Langmuir* **2010**, *26*, 9176–9178.
(106) Sposito, G. *The Surface Chemistry of Soils*; Oxford University Press: New York, 1984.
(107) Stumm, W. *Chemistry of the Interface Processes at the Mineral-Water*; John Wiley & Sons, Inc., 1992.
(108) Lee, S. S.; Fenter, P.; Park, C.; Sturchio, N. C.; Nagy, K. L. Hydrated Cation Speciation at the Muscovite (001)-Water Interface. *Langmuir* **2010**, *26*, 16647–16651.
(109) Park, C.; Fenter, P. A.; Sturchio, N. C.; Regalbuto, J. R. Probing Outer-Sphere Adsorption of Aqueous Metal Complexes at the Oxide-Water Interface with Resonant Anomalous X-Ray Reflectivity. *Phys. Rev. Lett.* **2005**, *94*, 076104.
(110) Lee, S. S.; Fenter, P.; Nagy, K. L.; Sturchio, N. C. Changes in Adsorption Free Energy and Speciation during Competitive Adsorption between Monovalent Cations at the Muscovite (001)-Water Interface. *Geochim. Cosmochim. Acta* **2013**, *123*, 416–426.
(111) Stillinger, F. H. Water Revisited. *Science* **1980**, *209*, 451–457.
(112) Marcus, Y. Thermodynamics of Solvation of Ions. *J. Chem. Soc., Faraday Trans.* **1991**, *87*, 2995–2999.
(113) Rubasinghege, G.; Grassian, V. H. Role(s) of Adsorbed Water in the Surface Chemistry of Environmental Interfaces. *Chem. Commun.* **2013**, *49*, 3071–3094.
(114) Wang, T.; Liu, Y.; Deng, Y.; Fu, H.; Zhang, L.; Chen, J. Adsorption of SO2 on Mineral Dust Particles Influenced by Atmospheric Moisture. *Atmos. Environ.* **2018**, *191*, 153–161.
(115) Fang, Y.; Tang, M.; Grassian, V. H. Competition between Displacement and Dissociation of a Strong Acid Compared to a Weak Acid Adsorbed on Silica Particle Surfaces: The Role of Adsorbed Water. *J. Phys. Chem. A* **2016**, *120*, 4016–4024.
(116) Mikhailov, E.; Vlasenko, S.; Martin, S. T.; Koop, T.; Pöschl, U. Amorphous and Crystalline Aerosol Particles Interacting with Water Vapor: Conceptual Framework and Experimental Evidence for Restructuring, Phase Transitions and Kinetic Limitations. *Atmos. Chem. Phys.* **2009**, *9*, 9491–9522.
(117) Wu, D.; Guo, X.; Sun, H.; Navrotsky, A. Energy Landscape of Water and Ethanol on Silica Surfaces. *J. Phys. Chem. C* **2015**, *119*, 15428–15433.
(118) Mazeina, L.; Navrotsky, A. Enthalpy of Water Adsorption and Surface Enthalpy of Goethite (α-FeOOH) and Hematite (α-Fe2O3). *Chem. Mater.* **2007**, *19*, 825–833.
(119) Lynden-Bell, R. M.; Rasaiah, J. C. From Hydrophobic to Hydrophilic Behaviour: A Simulation Study of Solvation Entropy and Free Energy of Simple Solutes. *J. Chem. Phys.* **1997**, *107*, 1981–1991.
(120) Szczerba, M.; Kalinichev, A. G.; Kowalik, M. Intrinsic Hydrophobicity of Smectite Basal Surfaces Quantitatively Probed by Molecular Dynamics Simulations. *Appl. Clay Sci.* **2020**, *188*, 105497.
(121) Szczerba, M.; Kuligiewicz, A.; Derkowski, A.; Gionis, V.; Chryssikos, G. D.; Kalinichev, A. G. Structure and Dynamics of Water-Smectite Interfaces: Hydrogen Bonding and the Origin of the Sharp O-Dw/O-Hw Infrared Band from Molecular Simulations. *Clays Clay Miner.* **2016**, *64*, 452–471.

TOC

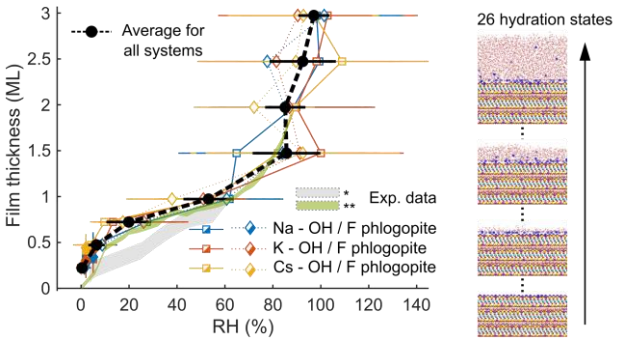
Average for
all systems
Exp. data
Na - OH / F phlogopite
K - OH / F phlogopite
Cs - OH / F phlogopite
Film thickness (ML)
RH (%)
26 hydration states